Testing for Welding, Joining or Additive Manufacturing Applications

Tanju Teker* and Ahmet Günes

Microstructure and mechanical properties of AISI 304/DUROSTAT 500 steel double-sided TIG welds

https://doi.org/10.1515/mt-2022-0033

Abstract: In this study, AISI 304 stainless steel and DUROSTAT 500 steel are combined using TIG double-sided arc welding. Microstructural differences of welded joints were researched by using a scanning electron microscope (SEM), an optical microscope, and electron backscattered diffraction. Mechanical properties of welded joints were investigated by microhardness, notch impact, and tensile tests. In addition, fracture surface morphology was evaluated using a SEM. The current power had a major impress on bead and hourglass shape. Maximum tensile resistance (677 MPa) was achieved at a welding time of 0.21 ($m \cdot min^{-1}$) at 460 (A) current, and the impact energy (116 J) was obtained. The weld metal consisted 41 wt% cementite, 25 wt% chromium carbide, 20 wt% martensite, and 14 wt% tetrataenite phases. With the increase in the current voltage, both bead and penetration sizes increased.

Keywords: AISI 304; DSAW; DUROSTAT 500; mechanical properties; microstructure.

1 Introduction

Stainless steels are indispensable materials in various industrial fields. Among the stainless steels, austenitic stainless steels (ASS) are the most preferred. This is because of the good weldability of ASS. It has high corrosion resistance, antibacterial properties, and machinability [1–3]. The welding quality is very notable in the manufacture of critical components such as boilers, petrochemical, and nuclear reactor components, where AISI 300 type steel is used [4]. DUROSTAT steels are steels with excellent machinability and wear resistance. There are steel grades DUROSTAT 400, DUROSTAT 450, and DUROSTAT 500. DUROSTAT 500 steels are the preferred materials for loader buckets, wagon bodies, conveyors, excavator components, road machinery, screens, and crusher components. These steels provide high resistance to mechanical wear [5–7]. Welding is used as an alternative instead of casting, bolted, and riveted manufacturing. The welding of steels is of great importance in the manufacturing industry [7, 8]. The TIG double-sided arc welding (DSAW) is a new method advanced to improve welding quality. It is an arc welding method in which the arc and the weld pool are formed between the tungsten electrode and the workpiece. The arc current directly affects penetration measurements, weld metal, and joint characteristics. It is the most important parameter of the welding process. The TIG welding produces high-quality welds with precise heat input control [9, 10]. Welded joining of stainless steels is one of the common methods applied. However, in the arc welding process, coarse grains and carbide formation occur along the grain boundaries in heat-affected zone (HAZ). The chromium-rich coarse structure and carbides adversely change the strength properties of the weld. In order to eliminate this disadvantage, the materials to be joined are usually joined by TIG welding. The amount of penetration varies in materials with different chemical compositions. The joints must have sufficient mechanical properties and quality. The strength of joints made by the TIG method depends on welding parameters such as weld seam shape, geometry, welding current, speed, and heat input [11–13]. Kwon and Weckman investigated the weldability of 1.5 mm-thick AA5182-O materials by the DSAW process. They achieved better standard welds than those manufactured using traditional welding joints [14].

In this study, AISI 304/DUROSTAT 500 steel was joined by TIG (DSAW) method without using additional wire and without welding edge preparation. The microstructure and mechanical characteristics of joints were researched experimentally.

***Corresponding author: Tanju Teker**, Faculty of Technology, Department of Manufacturing Engineering, Sivas Cumhuriyet University, 58140, Sivas, Turkey,
E-mail: tanjuteker@cumhuriyet.edu.tr
Ahmet Günes, Hasan Hüseyin Akdoğan Vocational and Technical Anatolian School, Gaziantep, Nizip, Turkey

Table 1: Nominal chemical composition of the AISI 304 and DUROSTAT 500 steels.

	Chemical compound (wt%)								
Materials	**C**	**Cr**	**Ni**	**Mn**	**Si**	**P**	**S**	**Mo**	**Fe**
AISI 304	0.08	18	8	2.00	1.00	0.04	0.03	–	Bal.
DUROSTAT 500	0.30	1.00	–	2.10	0.60	0.025	0.01	0.50	Bal.

2 Experimental procedure

AISI 304 and DUROSTAT 500 steel plates with dimensions of 10 × 100 × 1000 mm were used. The chemical composition contents of these materials are given in Table 1, and their mechanical properties are given in Table 2. The parameters used in the double-sided TIG welding method are given in Table 3. The joints were made using a Ge-Ka-Mak 500 AC/DC TIG welding machine.

The samples were sanded with 80–1200 mesh abrasives. The samples were polished with 3 µm diamond paste. The AISI 304 stainless steel side was electrolytically etched with a 50% alcohol + 50% HNO_3 solution at 12 V for 3–5 s. The DUROSTAT 500 steel side was etched with a 98% alcohol + 2% NHO_3 solution. The metallurgical structure was observed using an optical microscope (OM: LEICA DM750) and a scanning electron microscope (SEM: ZEISS EVO LS10). XRD analysis was performed using a Rigaku RadB-Dmax brand XRD device at CuKα, λ = 1.54059 Å wavelength. Electron backscattering diffraction (EBSD) analyses were performed to detect the crystallographic phase distribution. Hardness changes were made in QNESS Q10 brand device with 0.5 mm intervals under 100 g load. The tensile tests were performed on a 30 kN-capacity BESMAK branded tensile device at a tensile speed of 0.5 mm·min^{-1}. The image of the tensile test samples is presented in Figure 1. Notch impact tests were carried out using a 300 J hammer in BULUT brand notch impact tester. Details of the notch impact test samples are shown in Figure 2.

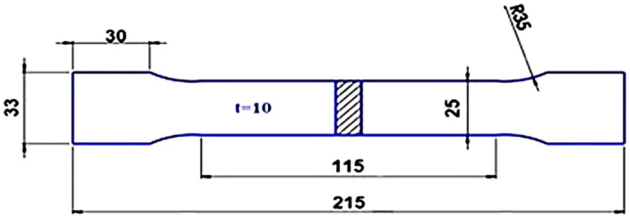

Figure 1: Image of the tensile test sample.

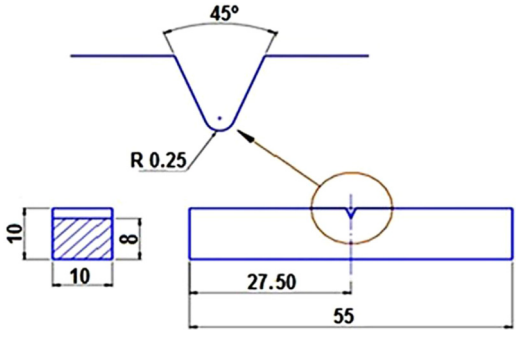

Figure 2: Detail of the notch impact test sample.

Table 2: Mechanical properties of the materials used in the experiments.

Materials	Tensile strength (MPa)	Yield strength (MPa)	Elongation (%)	Hardness (HB)
AISI 304	668	327	46	198
DUROSTAT 500	1550	1200	8	500

Table 3: Parameters used in welded joints.

Sample no.	Current intensity (A)	Arc voltage (V)	Shielding gas flow rate (l·min^{-1})	Welding speed (m·min^{-1})
S1	440	109	8	0.21
S2	450	112	8	0.21
S3	460	115	8	0.21

3 Experimental results

3.1 Macro and microstructure

The AISI 304/DUROSTAT 500 steels were joined without any problem by the TIG (DSAW) method without both additional wire and weld edge preparation. The weld seams and the cross-sectional views of the joints are given in Figures 3 and 4, respectively. The weld seams had a smooth crater structure. The increase in heat input in

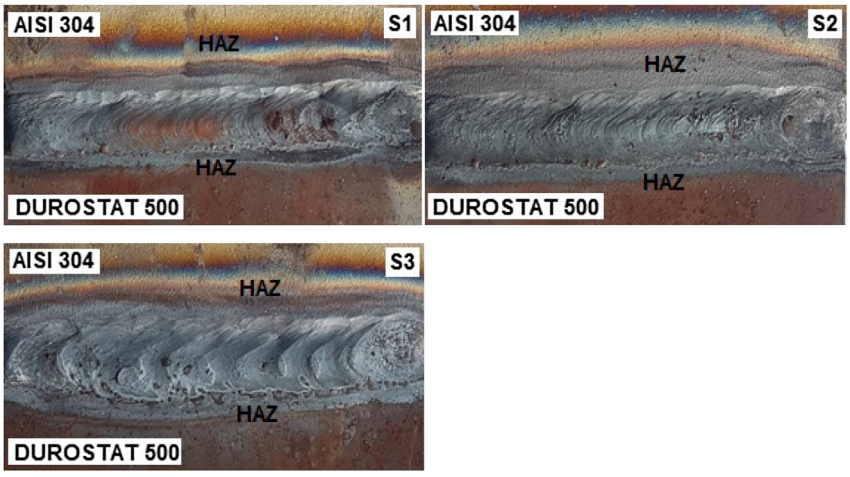

Figure 3: Weld seam view of the welded joints.

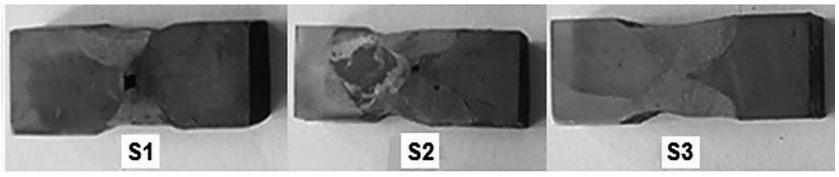

Figure 4: Weld section view of the welded joints.

parallel with the increasing current increased both the weld seam width and penetration. The distance between the seams had gradually decreased in mutual welds. At 460 A, the seams were joined by full contact with each other. The width of the HAZ-A side increased with increasing current. The welding arc tends toward the ferromagnetic material side [15]. Since AISI 304 is paramagnetic and DUROSTAT 500 is magnetic, more arc energy would accumulate on the DUROSTAT 500 side. This caused greater melting on the DUROSTAT 500 side. The increase in voltage increases the arc distance. The wide-arc distribution increases the weld width. Excess melting occurs on the surface. The welding stress has a direct effect on the geometry of the fusion zone and outer seam. An increase in tension creates a straighter seam, and the seam height decreases with an increase in welding tension [16].

The SEM and OM image of the microstructure of AISI 304/DUROSTAT 500 joints is given in Figures 5 and 6, respectively. No welding defect occurred at the weld seam interface. High heat input caused grain coarsening on the HAZ-A and HAZ-B sides. On the HAZ-A side, the grains were arranged in the rolling direction. Chromium carbides were formed at the grain boundaries. A dense carbide zone was formed on the AISI 304 side right next to the seam. These carbides are grain boundary carbides and are formed according to the formula Cr_xC_y. The white parts in the microstructure are austenite, and the black parts are δ-ferrite [17]. Figure 6 shows that the delta ferrite structure changed from lathy ferrite to skeletal ferrite in the weld zone. The structure in the weld region had an interdendritic ferrite in an austenite base structure. On the HAZ-A side, the weld transition zone was sharply separated from the weld pool. The transition zone on the HAZ-B side was wider. On the HAZ-B side, the structure consisted cementite + pearlite phases. According to the Schaeffler diagram, the weld metal consisted ($A + M + F(\delta)$) austenite, delta ferrite, and lath martensite phase dispersed in the austenitic matrix.

The top and bottom region EDS objects and values of the S3 sample are given in Figure 7 and Table 4, respectively. Fe, Cr, Mn, Ni, C, and Si were the prominent elements in the weld metal and base metal in the welded joints of AISI 304/DUROSTAT 500 steel. In the diffusion, the solution of carbon in solid and liquid alloy was dissimilar. When the low alloy steel and the weld pool come into contact with each other during the crystallization action, a diffusion state occurs around the weld metal. The solubility of C in DUROSTAT 500 and AISI 304 welds was varied. The carbon atoms in the high-carbon DUROSTAT 500 steel diffused into the stainless steel with a lower carbon content than the base material. The carbides in AISI 304 steel diffused the edge of the stainless steel weld. Chromium carbides formed near the weld. The heat input increased the dendrite size. Thus, the dendritic gaps and sizes in the weld metal have also increased. The formation of steep thermal gradients in the weld metal was the result of the relatively higher cooling rate. This allowed less time for the dendrites to grow. The cooling rate was slow at high heat

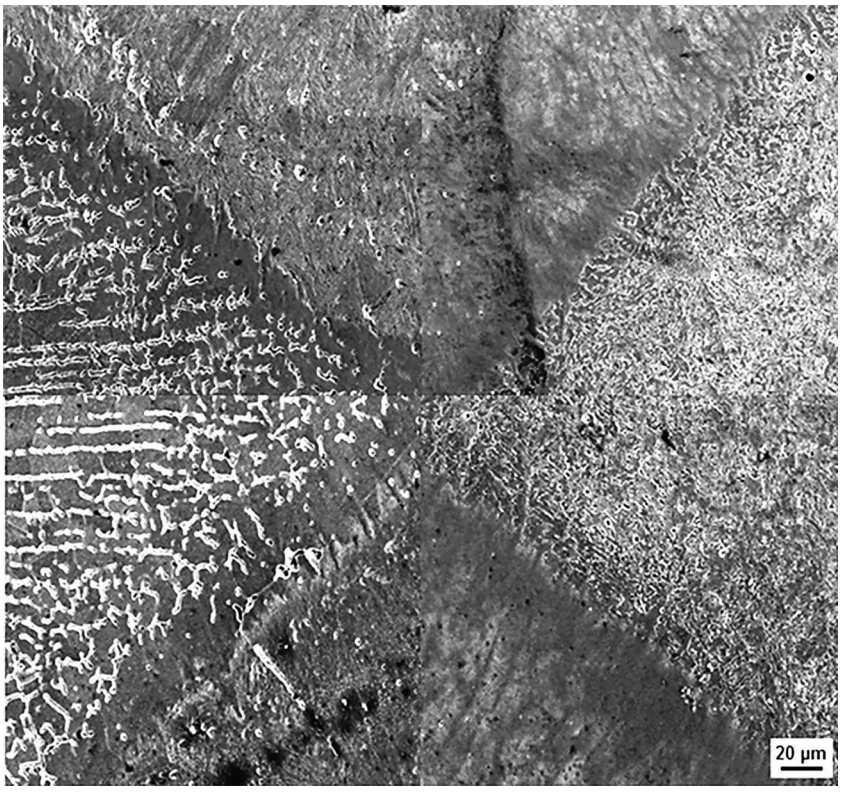

Figure 5: SEM image of the S3 joint.

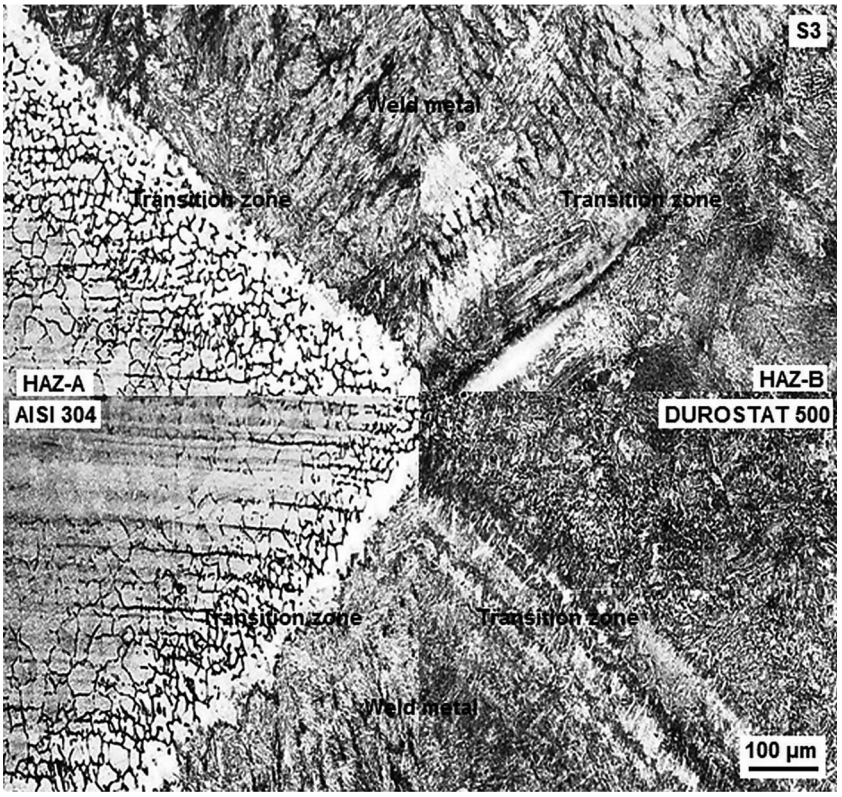

Figure 6: Optic image of the S3 joint.

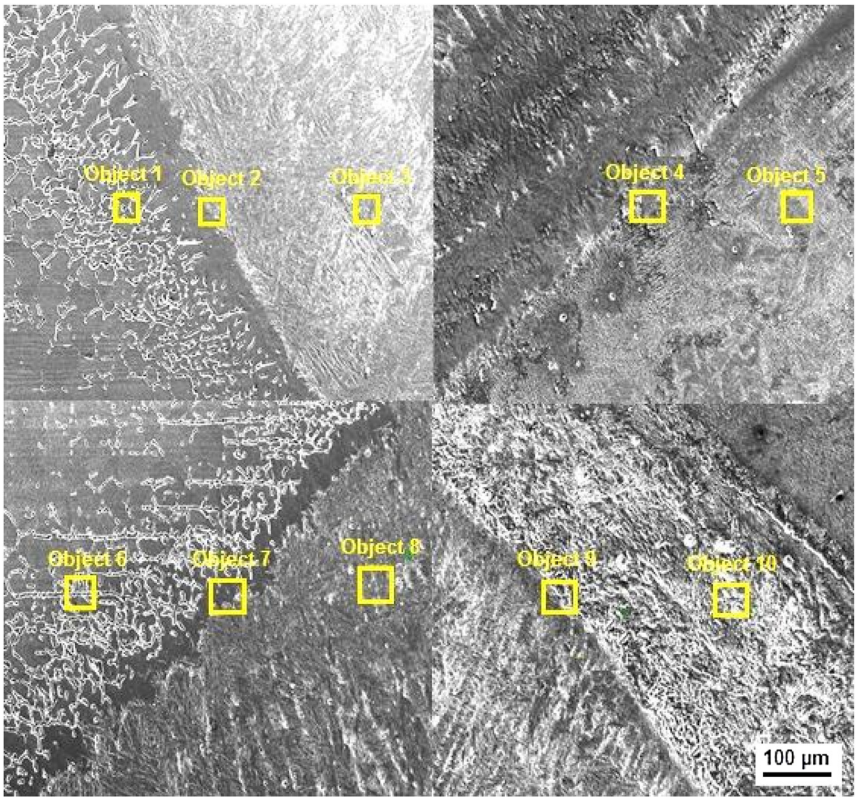

Figure 7: Top and bottom region EDS objects of the S3 sample.

Table 4: Top and bottom region EDS values of the S3 sample.

Sample no.	Analysis objects	Elements (wt%)					
		Fe	Cr	Ni	Mn	C	Si
S3	Object 1	50.83	19.65	7.91	16.30	4.99	0.31
	Object 2	55.40	15.53	6.45	17.07	5.03	0.52
	Object 3	60.66	10.73	4.62	18.54	4.70	0.75
	Object 4	68.02	1.74	1.04	22.41	6.29	0.50
	Object 5	69.68	0.89	0.75	22.50	5.52	0.65
	Object 6	50.38	19.67	8.17	16.65	4.68	0.45
	Object 7	53.68	15.75	6.58	17.11	6.37	0.51
	Object 8	59.16	10.65	4.46	19.34	5.84	0.55
	Object 9	65.02	4.88	2.17	20.79	6.77	0.36
	Object 10	64.94	0.70	0.64	21.53	11.78	0.41

input. This provided sufficient time for the dendrites to grow further into the fusion zone. The heat input experienced during the welding process was effective in the amount of δ-Fe. As the cooling rate increased, the δ-Fe content in the welds also increased [18].

X-ray analysis of the S3 sample is given in Figure 8. Martensite, Fe_3C, $CrFe_7C_{0.45}$, FeNi, Cr_3C_2, and Fe_3Ni_2 phases were formed.

The EBSD analysis of the S3 sample is given in Figure 9. The weld zone consisted 41 wt% cementite, 25 wt% chromium carbide, 20 wt% martensite, and 14 wt% tetrataenite phases. It was revealed that dense carbon atoms were spread from the base metal with a high carbon quantity to the weld area. In addition, the high chromium carbide ratio showed that the carbon in the weld metal was exposed to high temperature to form Cr_xC_y with the chromium element at high temperatures. The moving of grain orientations in the welds from their ideal position was due to the differential thermal gradient at the dendrite tip during solidification. Chromium and nickel were dispersed

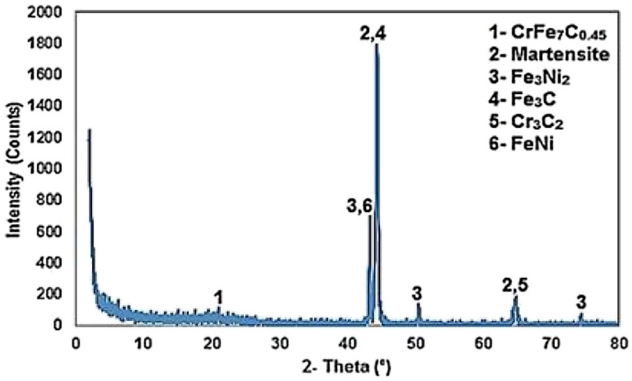

Figure 8: X-ray analysis of the S3 sample.

from the stainless steel to the DUROSTAT 500 steel. Iron and carbon were also diffused from the DUROSTAT 500 steel to the stainless steel. The presence of Ni and Cr in the melting zone was due only to the diffusion effects enhanced by the given linear energy.

Microhardness measurements are shown in Figure 10. The hardness values have changed in HAZ-A, HAZ-B, and weld metal; have decreased from the welding center to the base materials; and tended to decrease with the rise in joining current and heat input. The hardness in the weld center was higher than the hardnes of AISI 304 and DUROSTAT 500 steel. The existence of delta ferrite had a significant effect on the hardness of the weld pool [19, 20]. The average microhardness value of the weld zone was very close to each other. The hardness values on the HAZ-B side were slightly higher than that of the HAZ-A side. Due to the high carbon content of the main material on the HAZ-B side, carbon atoms diffused into this region. The hardness was high due to the formation of structures such as martensite and cementite as a result of rapid cooling during the solidification of the structure. It is known that the hardness of ferrite was higher than that of austenite. The reason for higher hardness on the weld metal and HAZ-B side was the higher Creq/Nieq and faster cooling rate. This was due to a lower fraction of austenite and a higher amount of chromium carbide precipitation in the weld metal. On the DUROSTAT 500 side, ferrite mixed with pearlitic structure predominated at the weld interface. Due to Cr and Ni, a twin structure was seen on the AISI 304 side with a mixture of austenite and some ferrite. During welding, the region close to the melting zone heats up rapidly at a temperature above the AC_3 point. On the

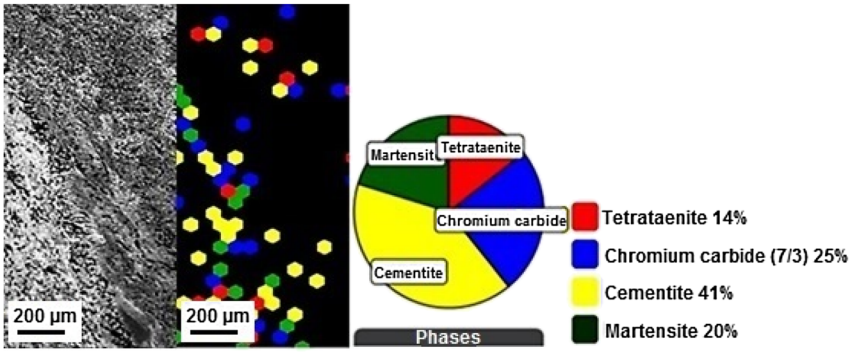

Figure 9: EBSD analysis of the S3 sample.

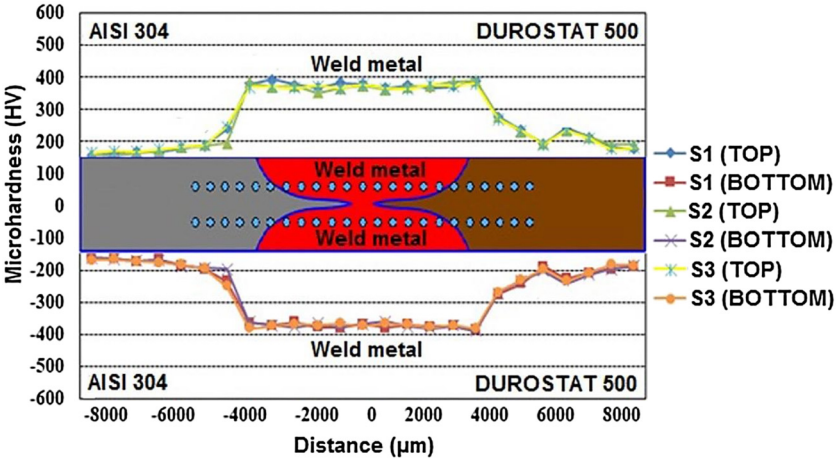

Figure 10: Microhardness results of samples S1, S2, and S3.

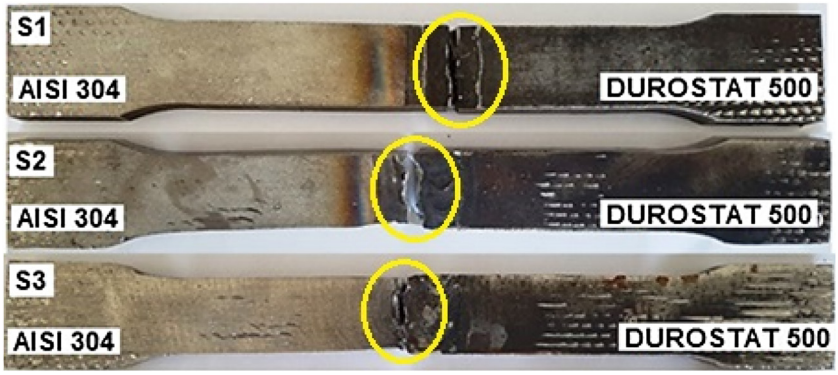

Figure 11: Photographs of the welded samples after the tensile test.

austenitic steel side, minor carbide precipitation and recrystallization of grains occurred. Ni and Cr migration events and rapid cooling condition formed martensite microstructure in the weld zone. It caused hardening of the heat-affected area. The HAZ hardness on the DUROSTAT 500 side gradually increased from 178 HV to 585 HV due to phase transformation. The HAZ hardness on the AISI 304 side was increased to about 245 HV. The change in hardness on the AISI 304 side was due to recrystallization, carbide precipitation, and ferrite appearing at grain boundaries.

3.2 Tensile test

The results of the tensile tests are displayed in Figure 11. The tensile strength values were determined as S1 = 642, S2 = 670, and S3 = 677 MPa. The gaps formed as a result of the weld seams not joining each other with full penetration caused a notch effect. The samples with full penetration were broken at the weld seam close to the AISI 304 base material. Depending on the increasing current intensity, the tensile strengths increased. The highest tensile strength was recorded in the S6 sample. The AISI 304 stainless steel was softer than the DUROSTAT 500 steel, which had a more brittle behavior. Stainless steel had five times the elongation of the DUROSTAT 500 steel. The HAZ of the carbon steel side was harder than the HAZ on the AISI 304 side. In the TIG welding process, a narrower weld area was created due to the lower heat value input at low amperage. For this reason, it is difficult to achieve perfect fusion at the melting point with too much diffusion to both sides. The higher the tensile strength, higher resistance to deformation of the S3 sample provided stronger weld metal. Mechanical properties are directly affected by the geometric appearance and size of the weld [20, 21]. High welding strength is due to the untempered martensitic and higher hardness in the weld pool. The ASS steel side and weld metal were prone to embrittlement by the presence of the sigma phase. The emergence of the sigma phase is between 600 and 900 °C, and the fastest occurs around 800 °C in austenitic-ferritic weld metals. As the arc current expands, the heat input increases and the cooling rate decreases, therefore, there is more time for microstructure development in the sigma-phase temperature range. As the current increases, the dispersion of the sigma phase in the weld zone and the HAZ increases. The sigma and carbide phases can act as the stress concentration for the fracture [19, 20]. At high current values, the samples were slag-free and combined with each other with full melting and penetration. The temperature of the AISI 304 side was high due to the strong fluidity of the molten pool due to the high heat input of the TIG process. During cooling after welding, some ferrite precipitated at the austenite grain boundaries.

3.3 Fracture surface analysis

The fracture surface image of the S3 sample is given in Figure 12. The homogeneous pits and cavities of various sizes and depths in the fibrous tissue showed ductile fracture.

Fractured surface EDS analysis of the S3 sample after tensile test is given in Figure 13. The EDS analysis values were found as at% values of elements for S3: Fe = 69.94, Cr = 22.83, and Ni = 7.22. There was Cr, Ni diffusion from the AISI 304 base metal to the weld metal. Also, the austenite/ferrite boundaries were the preferred sites for the precipitation of Cr_3C_2-type carbides. It had an embrittlement effect on the stainless steels. The sigma phase, nominally FeCr, was hard and brittle and occurred in bulky fractions, significantly reducing toughness and ductility.

3.4 Impact test

The fracture photographs of the samples after the notch impact test are given in Figure 14. With the increase in

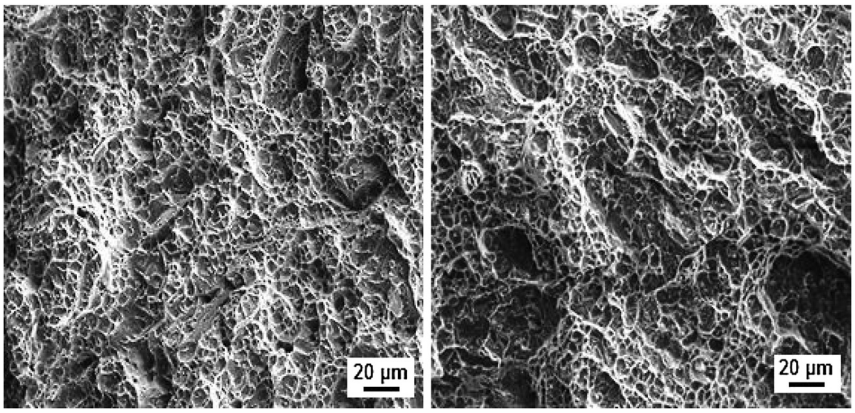

Figure 12: SEM fracture surface image of the S3 sample.

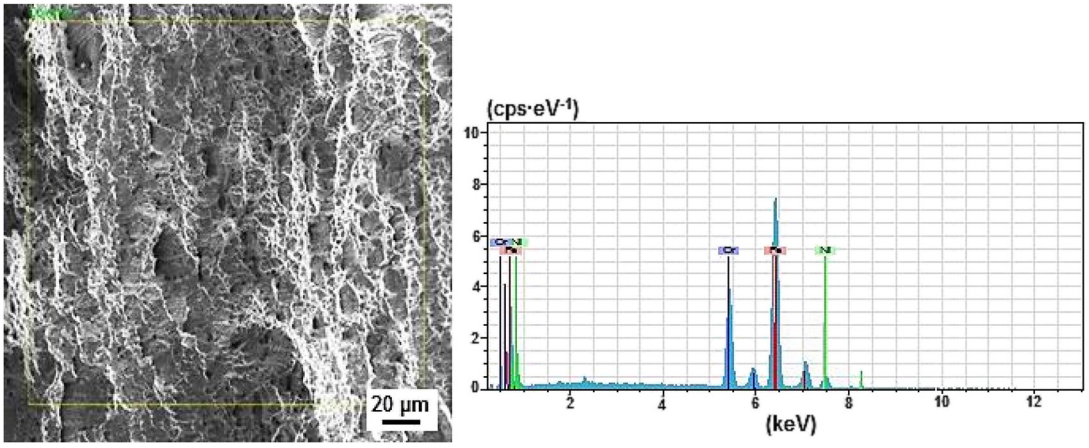

Figure 13: Fractured-surface EDS analysis of the S3 sample after tensile test.

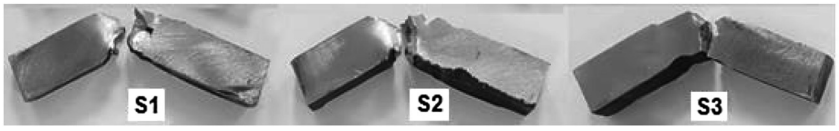

Figure 14: Fracture photographs of the samples after the notch impact test.

current intensity, the notch impact strength increased linearly. The notch impact results were obtained as: S1 = 68, S2 = 93, and S3 = 116 J. The heat input increased with the rise in the joining current. It enabled the expansion and deepening of the weld pool. With the increase in heat input, the sigma phase in the matrix increased. The CrC and σ-phases were formed in the joint of wear-resistant DUROSTAT 500 with AISI 304 stainless steel. These phases caused the stainless steel to become brittle [22]. The low impact strength could be attributed to both the precipitation of Cr_xC_y, the low fraction of austenite in the weld metal region. Increasing the amount of delta ferrite in the weld metals caused a decrease in the toughness of the welds against impacts.

4 Conclusions

The AISI 304/DUROSTAT 500 steel was joined by TIG-DSAW method without using additional wire and without welding edge preparation. The findings of the study are summarized as follows:

(1) The TIG-DSAW of AISI 304/DUROSTAT 500 steels achieved a good combination of joint, mechanical, and metallurgical properties.
(2) The penetration increased in parallel with the increasing amount of heat. At high current values, the samples were slag-free and combined with each other with full melting and penetration.

(3) The weld metal consisted ($A + M + F(\delta)$) austenite, delta ferrite, and lath martensite phase dispersed in the austenitic matrix.
(4) The weld metal consisted 41 wt% cementite, 25 wt% chromium carbide, 20 wt% martensite, and 14 wt% tetrataenite phases.
(5) High welding strength was due to the untempered martensite and higher hardness in the weld pool.
(6) The mechanical properties were directly affected by the geometric appearance and size of the weld. With an increase in current and voltage, the tensile properties improved.
(7) The impact strength increased linearly with the current intensity.
(8) The presence of delta-ferrite reduced ductility and potentially toughness.

Author contributions: All authors have accepted responsibility for the entire content of this submitted manuscript and approved submission.

Research funding: This study was supported by the Adıyaman University Scientific Research Project Unit (Grant number: MUFYL/2019-001).

Conflict of interest statement: The authors declare no conflicts of interest regarding this article.

References

[1] T. Sakthivel, M. Vasudevan, K. Laha et al., "Comparison of creep rupture behaviour of type 316L(N) austenitic stainless steel joints welded by TIG and activated TIG welding processes," *Mater. Sci. Eng., A*, vol. 528, nos. 22–23, pp. 6971–6980, 2011. https://doi.org/10.1016/j.msea.2011.05.052.

[2] H. Fujii, T. Sato, S. Lua, and K. Nogi, "Development of an advanced A-TIG (AA-TIG) welding method by control of marangoni convection," *Mater. Sci. Eng., A*, vol. 495, nos. 1–2, pp. 296–303, 2008. https://doi.org/10.1016/j.msea.2007.10.116.

[3] Y. Zhang, J. Huang, Z. Ye, Z. Cheng, J. Yang, and S. Chen, "Influence of welding parameters on the IMCs and the mechanical properties of Ti/Al butt joints welded by MIG/TIG double-sided arc welding-brazing," *J. Alloys Compd.*, vol. 747, pp. 764–771, 2018. https://doi.org/10.1016/j.jallcom.2018.03.119.

[4] J. J. Smith and R. A. Farrar, "Influence of microstructure and composition on mechanical properties of some AISI 300 series weld metals," *Int. Mater. Rev.*, vol. 38, no. 1, pp. 25–51, 1993. https://doi.org/10.1179/imr.1993.38.1.25.

[5] P. V. S. S. Sridhar, P. Biswas, and P. Mahanta, "Effect of process parameters on bead geometry, tensile and microstructural properties of double-sided butt submerged arc welding of SS 304 austenitic stainless steel," *J. BRAZ. SOC. MECH. SCI.*, vol. 42, pp. 551, 2020. https://doi.org/10.1007/s40430-020-02636-4.

[6] Y. M. Zhang, C. Pan, and A. T. Male, "Welding of austenitic stainless steel using double sided arc welding process," *Mater. Sci. Technol.*, vol. 17, no. 10, pp. 1280–1284, 2001. https://doi.org/10.1179/026708301101509205.

[7] C. Yang, H. Zhang, J. Zhong, Y. Chen, and S. Chen, "The effect of DSAW on preheating temperature in welding thick plate of high-strength low-alloy steel," *Int. J. Adv. Manuf. Syst.*, vol. 71, pp. 421–428, 2014. https://doi.org/10.1007/s00170-013-5287-0.

[8] W. Qiang and K. Wang, "Shielding gas effects on double-sided synchronous autogenous GTA weldability of high nitrogen austenitic stainless steel," *J. Mater. Process. Technol.*, vol. 250, pp. 169–181, 2017. https://doi.org/10.1016/j.jmatprotec.2017.07.021.

[9] Y. M. Zhang, C. Pan, and A. T. Male, "Improved microstructure and properties of 6061 aluminum alloy weldments using a double-sided arc welding process," *Metall. Mater. Trans.*, vol. 31, pp. 2537–2543, 2000. https://doi.org/10.1007/s11661-000-0198-8.

[10] A. Elmesalamy, J. A. Francis, and L. Li, "A comparison of residual stresses in multi pass narrow gap laser welds and gas-tungsten arc welds in AISI 316L stainless steel," *Int. J. Pres. Ves. Pip.*, vol. 113, pp. 49–59, 2014. https://doi.org/10.1016/j.ijpvp.2013.11.002.

[11] T. Teker, E. M. Karakurt, and F. Demir, "Mechanical property effects of symmetrical hour glass shapes formed during double-sided TIG keyhole arc welding of AISI1040 joints," *Mater. Test.*, vol. 59, no. 6, pp. 524–529, 2017. https://doi.org/10.3139/120.111041.

[12] Y. Feng, Z. Luo, Z. Liu, Y. Li, Y. Luo, and Y. Huang, "Keyhole gas tungsten arc welding of AISI 316L stainless steel," *Mater. Des.*, vol. 85, pp. 24–31, 2015. https://doi.org/10.1016/j.matdes.2015.07.011.

[13] S. Kumar and A. Shahi, "Effect of heat input on the microstructure and mechanical properties of gas tungsten arc welded AISI 304 stainless steel joints," *Mater. Des.*, vol. 32, no. 6, pp. 3617–3623, 2011. https://doi.org/10.1016/j.matdes.2011.02.017.

[14] Y. Kwon and D. C. Weckman, "Double sided arc welding of AA5182 aluminium alloy sheet," *Sci. Technol. Weld. Join.*, vol. 13, no. 6, pp. 485–495, 2008. https://doi.org/10.1179/174329308X271715.

[15] G. Lothongkum, P. Chaumbai, and P. Bhandhubanyong, "Study on the effects of pulsed TIG welding parameters on delta-ferrite content, shape factor and bead quality in orbital welding of AISI 316 L stainless steel plate," *J. Mater. Process. Technol.*, vol. 110, no. 2, pp. 233–238, 2001. https://doi.org/10.1016/S0924-0136(00)00875-X.

[16] R. Unnikrishnan, K. S. N. S. Idury, T. P. Ismail et al., "Effect of heat input on the microstructure, residual stresses and corrosion resistance of 304L austenitic stainless steel weldments," *Mater. Charact.*, vol. 93, pp. 10–23, 2014. https://doi.org/10.1016/j.matchar.2014.03.013.

[17] S. W. Shyu, H. Y. Huang, K. H. Tseng, and C. P. Chou, "Study of the performance of stainless steel A-TIG welds," *J. Mater. Eng. Perform.*, vol. 17, pp. 193–201, 2008. https://doi.org/10.1007/s11665-007-9139-7.

[18] K. H. Tseng and C. P. Chou, "Effect of pulsed gas tungsten arc welding on angular distortion in austenitic stainless steel weldments," *Sci. Technol. Weld. Join.*, vol. 6, no. 3, pp. 149–153, 2001. https://doi.org/10.1179/136217101101538686.

[19] J. C. Lippold and D. J. Kotecki, *Welding Metallurgy and Weldability of Stainless Steels*, New York, Wiley, 2005, pp. 80–120.
[20] V. J. Badheka, R. Basu, J. Omale, and J. Jzpunar, "Microstructural aspects of TIG and A-TIG welding process of dissimilar steel grades and correlation to mechanical behavior," *Trans. Indian Inst. Met.*, vol. 69, pp. 1765–1773, 2016. https://doi.org/10.1007/s12666-016-0836-5.
[21] T. Teker and D. Gencdogan, "Heat affected zone and weld metal analysis of HARDOX 450 and ferritic stainless steel double sided TIG-joints," *Mater. Test.*, vol. 63, no. 10, pp. 923–928, 2021. https://doi.org/10.1515/mt-2021-0022.
[22] F. J. Santos, G. B. Dutra, and T. V. Cunha, "Microstructural and mechanical evaluation of a dissimilar joining between SAE 1020 and AISI 304 steel obtained via ultra-high-frequency-pulsed GTAW," *J. Braz. Soc. Mech. Sci. Eng.*, vol. 41, p. 26, 2019. https://doi.org/10.1007/s40430-018-1534-5.

The authors of this contribution

Tanju Teker
Prof. Dr. Tanju Teker, born in 1971, works in the Manufacturing Engineering Department, Technology Faculty, Sivas Cumhuriyet University, Sivas, Turkey. He graduated from Metallurgy Education, Gazi University, Ankara, Turkey, in 1997. He received his M.Sc. and Ph.D. degrees from the Firat University, Elazig, Turkey, in 2004 and 2010, respectively. His research interests include metal coating techniques, fusion welding, and solid-state welding methods.

Ahmet Günes
Ahmet Günes, born in 1983, graduated from Metal Teacher, Zonguldak Karaelmas University, Turkey, in 2009. He received his M.Sc. degrees from Adıyaman University, Turkey, in 2020. He is currently studying in Hasan Hüseyin Akdoğan Vocational and Technical Anatolian School, Nizip, Gaziantep. His research interests include welding methods.